Three-dimensional polarized Monte Carlo atmospheric radiative transfer model (3DMCPOL): 3D effects on polarized visible reflectances of a cirrus cloud

Céline Cornet, Laurent Labonnote, Frédéric Szczap

Céline Cornet, Laurent Labonnote, Frédéric Szczap. Three-dimensional polarized Monte Carlo atmospheric radiative transfer model (3DMCPOL): 3D effects on polarized visible reflectances of a cirrus cloud. Journal of Quantitative Spectroscopy and Radiative Transfer, 2010, 111 (1), pp.174-186. 10.1016/j.jqsrt.2009.06.013 . hal-01971907

Three-dimensional polarized Monte Carlo atmospheric radiative transfer model (3DMCPOL): 3D effects on polarized visible reflectances of a cirrus cloud

C. Cornet [a,*], L. C-Labonnote [a], F. Szczap [b]

[a] *Laboratoire d'Optique Atmosphérique, UMR CNRS 8518, Université des Sciences et Technologies de Lille, Villeneuve d'Ascq, France*
[b] *Laboratoire de Météorologie Physique, UMR CNRS 6016, Université Blaise Pascal, Aubière, France*

ARTICLE INFO

Article history:
Received 12 December 2008
Received in revised form
9 June 2009
Accepted 19 June 2009

Keywords:
Radiative transfer
Polarization
3D cloud

ABSTRACT

A polarized atmospheric radiative transfer model for the computation of radiative transfer inside three-dimensional inhomogeneous mediums is described. This code is based on Monte Carlo methods and takes into account the polarization state of the light. Specificities introduced by such consideration are presented. After validation of the model by comparisons with adding-doubling computations, examples of reflectances simulated from a synthetic inhomogeneous cirrus cloud are analyzed and compared with reflectances obtained with the classical assumption of a plane parallel homogeneous cloud (1D approximation). As polarized reflectance is known to saturate for optical thickness of about 3, one could think that they should be less sensitive to 3D effects than total reflectances. However, at high spatial resolution (80 m), values of polarized reflectances much higher than the ones predicted by the 1D theory can be reached. The study of the reflectances of a step cloud shows that these large values are the results of illumination and shadowing effects similar to those often observed on total reflectances. In addition, we show that for larger spatial resolution (10 km), the so-called plane-parallel bias leads to a non-negligible overestimation of the polarized reflectances of about 7–8%.

1. Introduction

Modeling realistically and accurately interactions between solar radiation and atmospheric components is fundamental to assess radiative budget of the Earth and to correctly retrieve atmospheric components from remote sensing data. A review of all the different codes used to model radiative transfer inside atmosphere is beyond the scope of this paper but we can mention some of the most popular methods such as the discrete ordinate method [1,2], the adding-doubling method [3,4], the Successive order of Scattering method [5] or the Monte Carlo method [6,7]. Depending of their applications, some compute only reflectances and are called scalar method, others account for the polarization state of the light and are called vector method.

Neglecting the state of polarization of scattered light can lead to non-negligible errors, for example in case of Rayleigh scattering [8]. In addition, as interactions between light and scattering media modifies the polarization state of the light, it can be used to infer information on atmospheric components such as clouds or aerosols. Multi-angular polarimetric data can, for instance, be used to retrieve cloud phase [9,10], cloud particle size [11,12], information on cloud particle shape [13–15]. With this purpose, several spatial or airborne instruments measure or will measure in a near future polarized reflectances in several directions from UV to near-infrared wavelength.

---

* Corresponding author. Tel.: +33 3 20 61 91; fax: +33 3 20 43 43 42.
E-mail address: cornet@loa.univ-lille1.fr (C. Cornet).

The first spatial radiometer which was able to measure polarized light from space in the visible spectral range with up to 14 viewing directions, was the POLarization and Directionality of the Earth's Reflectance, POLDER [16], launched in 1996 on board ADEOS. It was followed by POLDER2/ADEOS2 in 2002 and by POLDER3/PARASOL which is flying in the A-train mission since 2005. Extended to the near-infrared range, two recent multi-viewing airborne polarimeters have been developed. The first one called OSIRIS (Observing System including polarization in the Solar infrared spectrum, [17]) was designed by the Laboratoire d'Optique Atmosphérique (LOA), in the continuation of POLDER; the second one RSP (Research Scanning Polarimeter) was designed by the Goddard Institute for Space Studies (GISS). In the near future, based on these airborne polarimeters, spatial version will be launched as, for example, the Aerosol Polarimeter Sensor (APS) on board the Glory mission [18].

To exploit these data, for practical reason and computational cost, most of the radiative transfer models used assume homogeneous plane parallel and infinite atmospheric layers (1D model). However, atmospheric components and more specifically clouds present lot of variabilities. Numerous papers have shown that neglecting 3D radiative transfer can lead to large errors in the computation of total directional reflectances and thus in the retrieval of some cloud properties (e.g. [19–24]). A review concerning "3D Radiative transfer in cloudy Atmosphere" can be found in the book of Marshak and Davies [25]. Most of the studies described in this book were done for water cloud but similar effects appear for ice clouds on fluxes [26–28] and thus probably on total reflectances. Until now, in our knowledge, no study concerning the effects of heterogeneity, fractional cover and finite dimensions of cloud on polarized reflectances were conducted. The only way to fill this lack in order to know the limitations of using a 1D cloud model to retrieve cloud properties from polarized reflectances is the simulation of interactions between cloud and polarized radiation in a three-dimensional approach.

In the solar spectral range, few different 3D radiative transfer models are used. One is the widely used code, SHDOM [29], based on a combination of spherical harmonic and discrete ordinate calculations. Others, for example based on wavelet approach, were developed to study more theoretically radiative heterogeneity effects and interaction between heterogeneity scales [30]. But, a large majority of 3D atmospheric radiative transfer models developed are based on Monte Carlo simulations [6]. They keep being continuously developed and improved [31,32] until the last one which is "an open source community code" (publicly available at http://i3rc.gsfc.nasa.gov/I3RC_community_model.htm, [33]). However, in the solar spectral range, no one account for the state of polarization.

In this paper, we describe a three dimensional and polarized radiative transfer Monte Carlo code based on a version that allowed to compute only total reflectances [24]. The paper is organized as follow. The second section reminds the general concept of radiative transfer with Monte Carlo method. In Section 3, we explain more specifically the vector approach, which allows to compute the polarization state of scattered light. Comparisons with 1D radiative transfer model are presented in Section 4 and finally results of a 3D simulations obtained from a synthetic cirrus cloud are shown and analyzed in Section 5. Conclusions are given in Section 6.

2. Standard radiative transfer Monte Carlo model: scalar approach

The radiative transfer model presented in this study follows the standard approach of a forward Monte Carlo model [34,35,6,7]. The 3D medium is defined in a Cartesian coordinates system $OXYZ$ with $N_X \times N_Y \times N_Z$ regular cubic cells containing the medium properties. For each scatterer in the model (molecules, aerosols or cloud), these properties are the extinction coefficient σ_{ext}, the single scattering albedo ϖ_0 and the phase function $p(\Theta)$.

Computation starts with a photon entering randomly at the top of the medium along the sun illumination direction defined by its zenithal and azimuth angle $(\theta_0;\varphi_0)$. The direction of travel is next given by the direction cosines: $u = \sin\theta_0 \cos\varphi_0$; $v = \sin\theta_0 \sin\varphi_0$ and $w = \cos\theta_0$. The photon is tracking cell by cell until it interacts or exits the medium.

The distance between two collisions is determined by the comparison of the photon optical path and the medium optical path. The photon optical path is determined from the Beer–Lambert law using the final expression:

$$\tau_{photon} = -\ln(\zeta) \tag{1}$$

where ζ is an uniform random number between 0 and 1.

The medium optical path τ_{medium} that travels the photon, corresponds to the sum of successive different cell optical thickness:

$$\tau_{medium} = \tau_{cell_1} + \tau_{cell_2} + \cdots + \tau_{cell(coll)} \tag{2}$$

where τ_{cell_i} corresponds to the optical thickness in the ith crossed cell and $\tau_{cell(coll)}$ corresponds to the optical path integrated between the edge of the last crossed cell and the point where the collision happens.

A cell optical path is computed from the extinction coefficient times the distance l between the photon position and the nearest boundary along the direction of propagation. Eq. (2) can then be also written:

$$\tau_{medium} = \sigma_{cell_1} l_1 + \sigma_{cell_2} l_2 + \cdots + \sigma_{cell(coll)} l_{coll} \tag{3}$$

Numerically, that means comparing τ_{photon} and τ_{cell_i} for each crossed cell.

If $\tau_{photon} > \tau_{cell_i}$, the photon reaches the boundary without interacting with the medium and its coordinates are updated as follow:

$$\begin{cases} x' = x + ul \\ y' = y + vl \\ z' = z + wl \end{cases} \tag{4}$$

and the photon optical path is adjusted as follows: $\tau'_{photon} = \tau_{photon} - \tau_{cell_i}$.

Otherwise if $\tau_{photon} < \tau_{cell_i}$, there is collision inside the cell, the new coordinates of the photon are computed using $\tau_{photon}/\sigma_{cell}$ instead of l in Eq. (4) and the code runs trough different steps:

(i) The type of particles (molecules, aerosols or cloud) is determined from a random number between 0 and 1 and a probability law computed from the cell extinction coefficient of each type of particles.

(ii) If the medium is absorbing, the weight W of the photon equal to unity when the photon enters in the domain, is simply multiply by the single scattering albedo of the scatterer. When the weight reaches a value below 10^{-6}, the photon is considered completely absorbed by the medium, its tracks stop here and a new photon is launched.

(iii) The new direction of the photon is determined from two angles in the photon coordinates system. The scattering azimuth angle ϕ is chosen randomly between $[-\pi;\pi]$ and the scattering zenithal angle Θ is obtained from its cumulative probability function which is computed from the phase function of the particles (see Section 3.1). The new direction of the photon (u', v', w') is computed from the previous direction (u, v, w) and the scattering angles (Θ, ϕ) using [34]

$$\begin{cases} u' = (bcwu - bdv)/\sqrt{(1-w^2)} + au \\ v' = (bcwv + bdu)/\sqrt{(1-w^2)} + av \\ w' = -bc\sqrt{1-w^2} + aw \end{cases} \tag{5}$$

where $a = \cos\Theta$; $b = \sqrt{1-a^2}$; $c = \cos\phi$ and $d = \sqrt{1-c^2}$.

(iv) To speed up the code, the local estimate method [6,7] is used to compute the average reflectances in a specified direction. This method computes the contribution L_n of the nth scattering event reduced by the attenuation of the medium till the top of the atmosphere in the viewing direction (θ_v, φ_v):

$$L_n(x,y) = W_n \frac{p(\Theta_v)}{4\pi} \exp[-\tau_{medium}(z, \theta_v, \varphi_v)] \tag{6}$$

where $p(\Theta_v)$ is the phase function of the scatterer and Θ_v the scattering angle between the direction followed by the photon and the output viewing direction (θ_v, φ_v).

The contribution of the surface is computed in the same way either considering an isotropic reflection defined by the surface albedo or an ocean reflection characterized by a bi-directional reflectance function. From it, a cumulative probability function is computed at the beginning of the code to obtain the reflection angles (Θ, ϕ).

After the treatment of a scattering event, the photon is tracked to the next scattering event and this until it exits the medium. A new photon is then launched and the whole process is runs again.

At the end of the simulation, when all the photons are computed, the total contribution for each pixel is normalized by the factor $N_{photons}/\pi N_x N_y$ in order to obtain as output a normalized reflectance noted:

$$I = \frac{\pi.R}{\mu_0 F_0} \times 100 \tag{7}$$

where R is the reflected radiance in W m^{-2} sr^{-1} and $\mu_0 F_0$ the incoming solar flux. This code in its scalar approach was extensively compared with SHDOM [29] on I3RC cases [33] and gave accurate results.

3. Polarized radiative transfer Monte Carlo model: vectorized approach

Excepted some differences, the general scheme of the vector approach is similar to those of the scalar approach. In the scalar scheme, scalar quantities, e.g. radiances, are computed whereas in the polarization scheme, we compute the Stokes vector $S = (I, Q, U, V)$ that completely describe the polarized state of the light [8]. The phase function is therefore substituted by the 4×4 phase matrix $P(\Theta)$ which, in case of spherical particles, is computed from the Mie theory. Others important differences concern the computation of the scattering azimuth angle and the rotation of the electric field characterizing the polarization. Note that, so far, the polarized 3D model presented in this paper allows only the computation of reflectances from a medium composed of randomly oriented particles. Some modifications will be include later in order to allow computation of oriented particles.

3.1. *Computation of the scattering azimuth angle (ϕ)*

One important difference between the scalar and the vector approach comes from the computation of the scattering azimuth angle for each scattering event. In the scalar approach, this angle is chosen randomly between $-\pi$ and π, which means that the probability density function (PDF) of ϕ is characterized by a simple uniform distribution. In the vector approach, the scattering azimuth angle ϕ depends on the scattering zenithal angle Θ and on the state of polarization of the incident photon. The uniform PDF of ϕ is replaced by a conditional PDF $f(\phi|\Theta)$, which is the probability of ϕ given Θ. In order to give the expression of this conditional PDF, we will use, in this sub-section, the expression of the electric field E characterizing the state of polarization and the amplitude matrix $A(\Theta)$. They are obviously related, respectively, to the Stokes vector S and to the phase matrix $P(\Theta)$ [3].

Let us consider the coordinate system linked to the photon before a scattering event $Oxyz$ where $\vec{oz}$ is along the incident photon direction (Fig. 1). In this system, the incident electric vector is expressed in the Oxy plane and the incident energy I_i is given by

$$I_i = E_x E_x^* + E_y E_y^* = I_x + I_y \tag{8}$$

Here, the electric field is a complex number and the asterisk stands for the conjugate quantity. For simplicity, we assume that the incident photon energy is 1: $I_x + I_y = 1$.

A scattering event stands in the scattering plane defined from the incident and scattered directions. The new direction of the photon is characterized by the

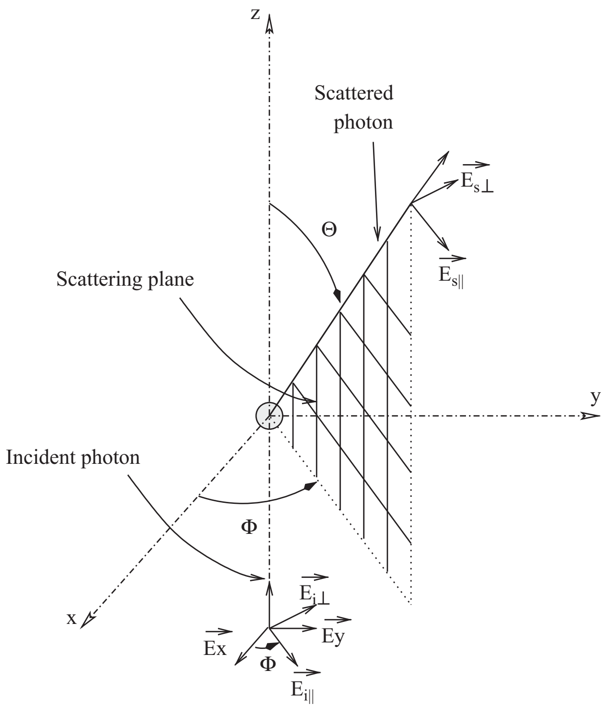

Fig. 1. Definition of the geometry used to describe the scattering event of an incident photon by a atmospheric particle.

scattering angles (Θ, ϕ) in the coordinate system linked to the incident photon *Oxyz* which is different of the coordinate system *OXYZ* linked to the medium. The rotation matrix allowing to move from one to another coordinate systems is given in Section 3.2.

The incident electric field, in the coordinate system linked to the scattering plane is then (Fig. 1):

$$\begin{cases} E_{i\parallel} = \cos\phi E_x + \sin\phi E_y \\ E_{i\perp} = -\sin\phi E_x + \cos\phi E_y \end{cases} \tag{9}$$

where $E_{i\parallel}$ and $E_{i\perp}$ are the components of the incident electric field, respectively, parallel and perpendicular to the scattering plane.

After a scattering event, the scattered electric vector is given by

$$\begin{pmatrix} E_{s\parallel} \\ E_{s\perp} \end{pmatrix} = \begin{pmatrix} A_2 & 0 \\ 0 & A_1 \end{pmatrix} \begin{pmatrix} E_{i\parallel} \\ E_{i\perp} \end{pmatrix} = \begin{pmatrix} A_2 E_{i\parallel} \\ A_1 E_{i\perp} \end{pmatrix} \tag{10}$$

A_1 and A_2 being the coefficients of the matrix amplitude of a randomly oriented scatterer or of spherical particles.

The scattered intensity can be written from Eq. (9), (10) as

$$\begin{aligned} I_s(\Theta, \phi) &= E_{s\parallel}E^*_{s\parallel} + E_{s\perp}E^*_{s\perp} \\ &= |E_x|^2(\cos^2\phi|A_2(\Theta)|^2 + \sin^2\phi|A_1(\Theta)|^2) \\ &\quad + |E_y|^2(\sin^2\phi|A_2(\Theta)|^2 + \cos^2\phi|A_1(\Theta)|^2) \\ &\quad + (E_xE^*_y + E^*_xE_y)\sin\phi\cos\phi(|A_2(\Theta)|^2 - |A_1(\Theta)|^2) \end{aligned} \tag{11}$$

Moreover, the flux scattered in the solid angle $d\Omega = \sin\Theta\, d\Theta\, d\phi$ in the direction (Θ, ϕ) is

$$I_s(\Theta, \phi)\, d\Omega = f(\Theta, \phi)\, d\Theta\, d\phi \tag{12}$$

where $f(\Theta, \phi)$ called the joint probability of Θ and ϕ is the PDF of the photon being scattered following the angle (Θ, ϕ).

From Eqs. (11) and (12), this PDF is written as

$$\begin{aligned} f(\Theta, \phi) = {} & I_x\cos^2\phi|A_2(\Theta)|^2\sin\Theta + I_x\sin^2\phi|A_1(\Theta)|^2\sin\Theta \\ & + I_y\sin^2\phi|A_2(\Theta)|^2\sin\Theta + I_y\cos^2\phi|A_1(\Theta)|^2\sin\Theta \\ & + U_i\sin\phi\cos\phi(|A_2(\Theta)|^2 - |A_1(\Theta|^2)\sin\Theta \end{aligned} \tag{13}$$

where $I_x = |E_x|^2$, $I_y = |E_y|^2$ and the third component of the incident Stokes vector $U_i = E_xE^*_y + E^*_xE_y$.

This joint PDF of Θ and ϕ can also be written as the product of the prior PDF of $\Theta, f_\Theta(\Theta)$ with the conditional PDF of ϕ given $\Theta, f(\phi|\Theta)$

$$f(\Theta, \phi) = f_\Theta(\Theta) f(\phi|\Theta) \tag{14}$$

As $I_x + I_y = 1$, we can easily compute $f_\Theta(\Theta)$ as follow:

$$f_\Theta(\Theta) = \int_0^{2\pi} f(\Theta, \phi)\, d\phi = \pi\sin\Theta(|A_1(\Theta)|^2 + |A_2(\Theta)|^2) \tag{15}$$

In this expression, one can identify the so called phase function $p(\Theta) = (|A_1(\Theta)|^2 + |A_2(\Theta)|^2)$. From $f_\Theta(\Theta)$, it is easy to compute the cumulative distribution function $F_\Theta(\Theta)$:

$$F_\Theta(\Theta) = \frac{\int_0^\Theta f_\Theta(\Theta)\, d\Theta}{\int_0^\pi f_\Theta(\Theta)\, d\Theta} = \frac{L(\Theta)}{L(\pi)} \tag{16}$$

The zenithal angle Θ is found by resolving the following equation:

$$L(\Theta) = \zeta_\Theta L(\pi) \tag{17}$$

where ζ_Θ is an uniform random number between 0 and 1.

Once we get Θ, we can compute the cumulative conditional distribution function of ϕ as

$$F(\phi|\Theta) = \frac{\int_0^\phi f(\phi|\Theta)\, d\phi}{\int_0^{2\pi} f(\phi|\Theta)\, d\phi} \tag{18}$$

With the second component of the Stokes vector, $Q_i = I_x - I_y$ and the degree of polarization

$$D_p(\Theta) = \frac{|A_1(\Theta)|^2 - |A_2(\Theta)|^2}{|A_1(\Theta)|^2 + |A_2(\Theta)|^2} = -\frac{P_{12}(\Theta)}{P_{11}(\Theta)}$$

Eqs. (13), (14), (15) and (18) give

$$F(\phi|\Theta) = \frac{\phi}{2\pi} - \frac{1}{2\pi}\left(\frac{\sin 2\phi}{2}Q_i + U_i\sin^2\phi\right)D_p(\Theta) \tag{19}$$

and the azimuth angle ϕ is found by resolving

$$2\pi\zeta_\phi = \phi - \left(\frac{\sin 2\phi}{2}Q_i + U_i\sin^2\phi\right)D_p(\Theta) \tag{20}$$

where ζ_ϕ is an uniform random number between 0 and 1.

Once we get the scattering angles Θ and ϕ, the new direction of the photon is computed following Eq. (5). Note that $2\pi\zeta_\phi = \phi$ is the way to obtain ϕ when the polarization is not considered (scalar approach). Fig. 2 presents the cumulative distribution function of ϕ in the case of Rayleigh scattering for both scalar and vector approach and for different zenithal angles. The vector approach introduces oscillation around the straight line

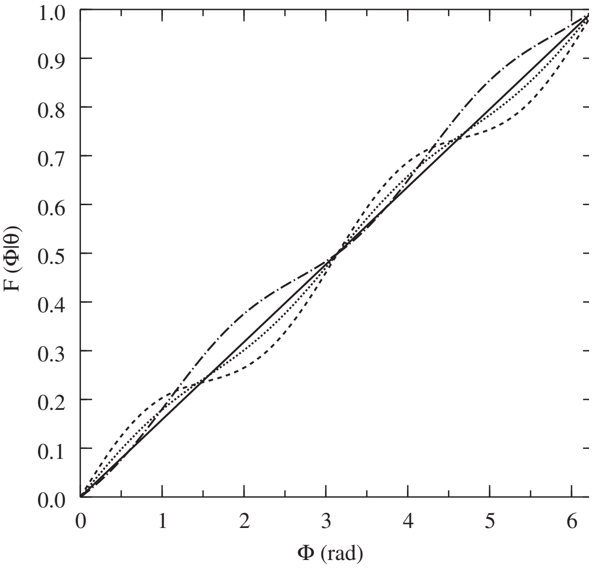

Fig. 2. Cumulative distribution function of the scattering azimuth angle ϕ in case of Rayleigh scattering with the scalar approach (solid line) and with the vector approach for $\Theta = 140^\circ$ (dotted line) and for $\Theta = 90^\circ$ for different incident Stokes vector (dashed and dot-dashed line).

that is given by the scalar approach. Depending of the zenithal angle (Θ) and the degree of polarization of the incident beam, these oscillations are more or less important and can introduce important differences on the reflectances. Note also that other ways can be use to find the azimuth angle, for example the rejection method [36].

3.2. Scattering and rotation of the Stokes vector

As already mentioned, another important difference in the vector approach concerns the modification of the coordinate system when a scattering event happens. Indeed, the Stokes vector S is defined with respect to a reference plane, which here is the meridian plane defined as in [8] by the vertical direction Oz and the direction of propagation. However, in order to compute the change in polarization, the Stokes vector needs to be expressed in the scattering plane before to be multiplied by the particle scattering matrix (Fig. 1). Therefore, we have to perform: (i) a first rotation to express the incident Stokes vector (S_i) in the scattering plane; (ii) to multiply it by the particle scattering matrix ($\mathbf{P}$) to obtain the scattered Stokes vector in the scattering plane; and (iii) to perform a second rotation to express this new vector (S_s) in the new meridian plan defined by Oz and the new direction of propagation (Fig. 3). Therefore, in order to perform a scattering from the incident direction defined by (θ, φ) to a new direction defined (θ', φ'), the incident Stokes vector S_i must be multiplied the matrix Z [3,36]:

$$Z(\theta, \theta', \varphi - \varphi') = R(\pi - i_2)P(\Theta)R(-i_1) \tag{21}$$

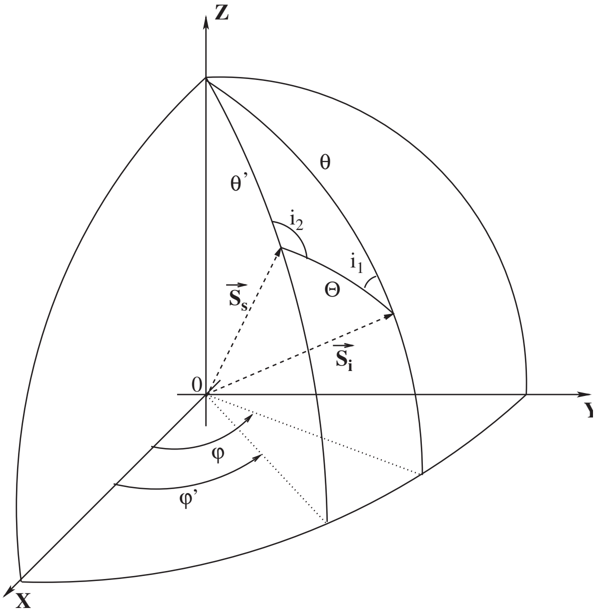

Fig. 3. Geometry of a scattering event. S_i and S_s are, respectively, the incident and the scattered Stokes vector.

where Θ is the zenithal scattering angle and i_1 and i_2 two rotation angles defined as follows (Fig. 3) [37,3]:

$$\begin{aligned} \cos i_1 &= \cos\varphi \\ \cos i_2 &= \frac{-\cos\theta + \cos\theta' \cos\Theta}{\pm \sin\Theta \sin\theta'} \end{aligned} \tag{22}$$

The sign ± depends of the sign of $(\varphi - \varphi')$. Note that $\lim_{\Theta \to 0} \cos i_2 = 1$ and $\lim_{\theta' \to 0} \cos i_2 = \pm\cos(\varphi - \varphi')$

The rotation matrix R is given by

$$\mathbf{R}(i) = \begin{pmatrix} 1 & 0 & 0 & 0 \\ 0 & \cos 2i & \sin 2i & 0 \\ 0 & -\sin 2i & \cos 2i & 0 \\ 0 & 0 & 0 & 1 \end{pmatrix} \tag{23}$$

4. Total and polarized reflectances in case of homogeneous clouds (1D)

4.1. Validation of the MC polarized model

In our knowledge, there is no available 3D atmospheric model accounting for the state of polarization of the light in the visible part of the spectrum. It is thus difficult to validate our model directly. But, as it was already validated with success for total reflectances on 3D cloud, here we tested the account of the polarization state on 1D homogeneous cases. Several comparisons were made with the well-known Adding-Doubling code [4]. We present the results obtained for a homogeneous cirrus cloud with an optical thickness 2 located between 7 and 9 km. The phase matrix used comes from the IHM (Inhomogeneous Hexagonal Monocrystal) model [38]. The sun incidence is 60° and results are presented in Fig. 4 for different view zenithal angles (0°, 30° and 60°) and for different view

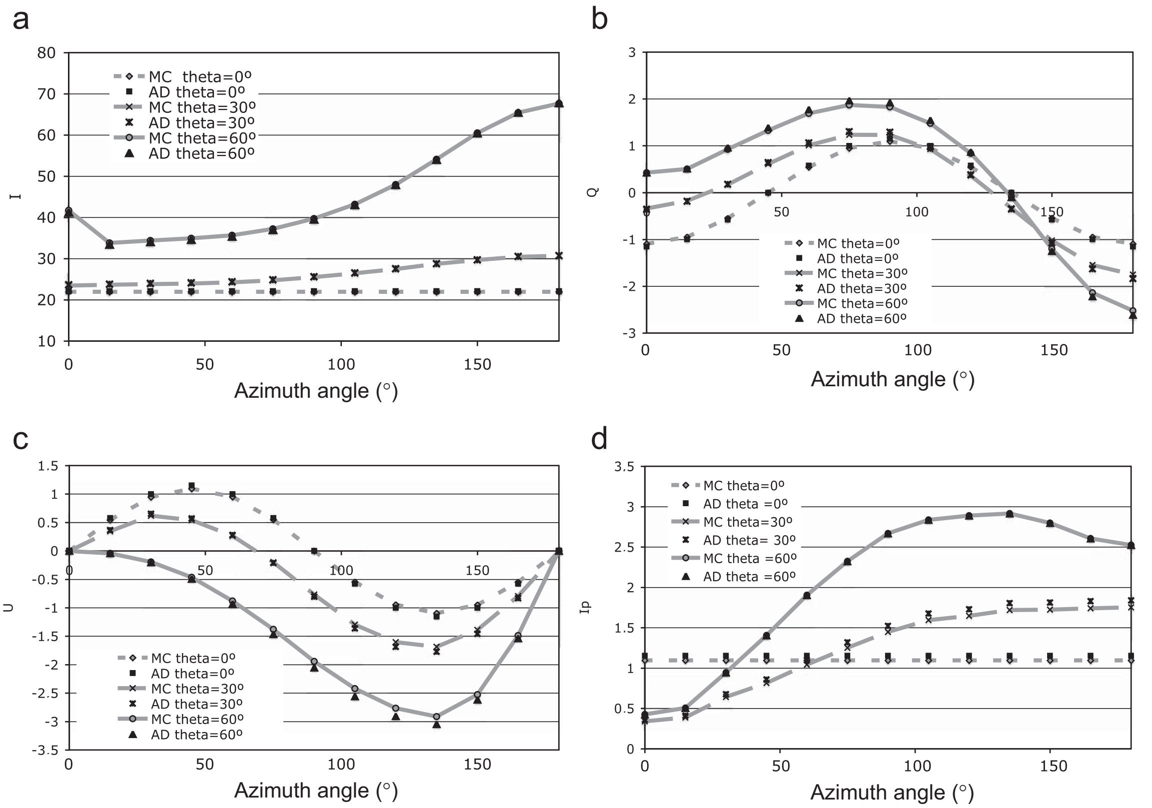

Fig. 4. Comparisons of the Stokes parameters computed with the Monte Carlo code (MC) and an Adding-Doubling code (AD). $\theta_s = 60^\circ$, $\theta_v = 0^\circ$, 30° or 60° and φ_v between 0° (backward) and 180° (forward): (a) I; (b) Q; (c) U; and (d) I_p. The Stokes parameters and the reflectances are in percent.

azimuth angles between 0° (backward scattering) and 180° (forward scattering). The last component V is usually very small, we present thus results only for the first three components of the Stokes vector (I, Q, U). We add also comparisons obtained for the polarized reflectance I_p that is commonly used in retrieval algorithms. This quantity describes the amount of polarized light:

$$I_p = \varepsilon\sqrt{Q^2 + U^2 + V^2} \tag{24}$$

where $\varepsilon = \pm 1$ represents the sign of the polarized reflectances [38].

These comparisons between the two models give very similar results: the error is below ±1% for I and about ±4−5% for Q, U and I_p. The differences observed for Q, U and I_p can be explained firstly by the small values reached by the polarized reflectances and secondly by the treatments of the phase matrix in the two models. In the Monte Carlo model, the exact phase matrix is used whereas in the Adding-Doubling code a decomposition in Legendre polynomials is done. This can introduce some approximations. Comparisons made with Rayleigh phase function confirm this latter hypothesis. Indeed, in this case, exact formula for Legendre polynomials decomposition is known and differences obtained are below 1% for both I and I_p even for cloud optical thickness of 5.

Comparisons have been done only for homogeneous cloud cases but as the polarized Monte Carlo model gives accurate results for polarized reflectances over homogeneous cloud and for total reflectances over 3D cloud scene, we are confident on results obtained for both total and polarized reflectances above 3D scenes.

4.2. *Reflectances of homogeneous clouds*

Fig. 5 presents, for homogeneous cloud, total and polarized reflectances in function of optical thicknesses for a zenithal observation angle of 30° and an azimuth angle of 180°. This direction corresponds to the forward scattering where the polarization by the particles is important. Under the homogeneous assumption (solid line), we recognize the well-known non-linear relationship between reflectances and optical thickness. This non-linear relationship exists for both total and polarized reflectances but as already pointed out, we note that the saturation of the polarized reflectances appears for a relatively small optical thickness of about 3. This is because the final polarization state comes from the first few orders of scattering. This particularity is fundamental and makes very useful the polarized measurements in order to retrieve information on particle shapes or size. Indeed, as polarized reflectances are less sensitive to multiple scattering, information contained in the measurement comes essentially from the particles scattering properties via their phase matrix.

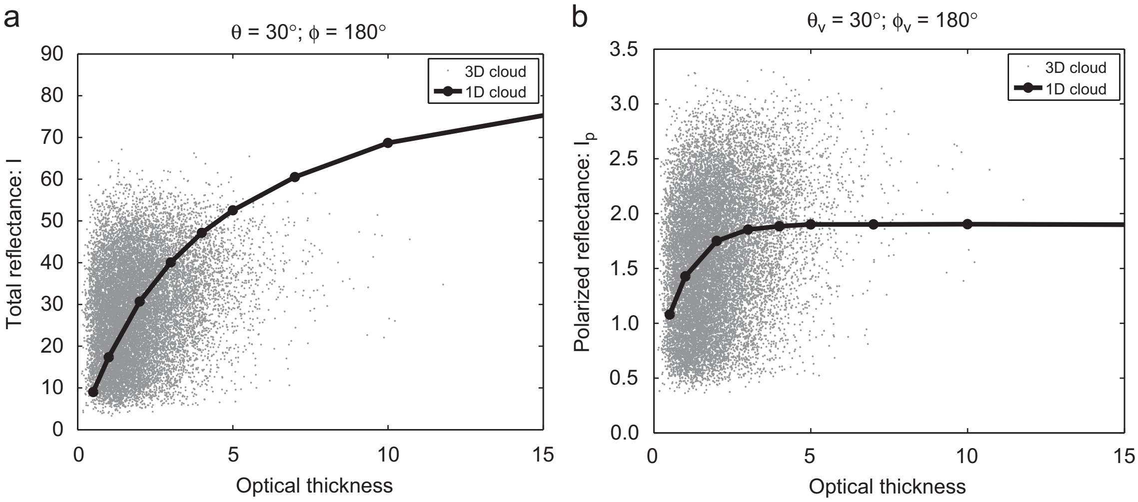

Fig. 5. Total (a) and polarized (b) reflectances in percent in function of optical thickness computed for homogeneous cirrus clouds (solid line) and for the heterogeneous cirrus cloud presented in Fig. 6 (dot) with $\overline{\tau} = 2$.

5. A polarized 3D cloud case

For the reasons cited above, information of polarized reflectances is often used for microphysical ice cloud purposes. Therefore, as example in this paper, we choose to study the heterogeneity effects on polarized reflectances of a inhomogeneous cirrus cloud. The cloud was simulated with a stochastic cloud model described in the Section 5.1. Results of radiative transfer are shown in Section 5.2 and an highlight on 3D effects on polarized and non-polarized reflectances is presented in Section 5.3.

5.1. The 3D cloud model: 3DCloud

In order to analyze cloud radiative properties as a function of their optical properties, we need to generate 3D synthetic inhomogeneous cloud fields sharing statistical and geometrical properties of real clouds. The algorithm used must be fast and flexible, in such way that clouds properties can be chosen by the user. In radiative transfer community, inhomogeneous clouds generators are often based either on fractal [39] or Fourier [40] or wavelet [41] framework in order to set cloud scale invariant properties, which result mathematically in a one dimensional spectral slope in Fourier space equal to $-\frac{5}{3}$. Excepted the model Clougen [42] which is based on a Fourier algorithm that mimics fallstricks of cirrus, the main drawback of these approaches is that they cannot take into account the effects of non-linear physical processes such as cell convection, advection or wind shear. On contrary, in atmospheric mesoscale modeling community, inhomogeneous clouds can be simulated with the help of large Eddy simulations (LES) or cloud resolving model (CRM) and physical processes are accounted for. Nevertheless, CPU time is prohibitive and clouds scale invariant properties, especially at small scale, are often not respected.

In this paper, we used a fast 3D cloud generator called 3DCloud [43] that is able: (i) to take into account dynamical and thermodynamical processes effects on 3D cloud structures; (ii) to set the scale invariant properties at small scale; and (iii) to set the optical statistical properties (probability density function, inhomogeneous parameter describing the intensity of cloud inhomogeneity [44], cloud coverage...) in a very flexible way.

The algorithm used to generate 3D clouds can be divide into two steps:

- The first step consists in generating 3D ice mixing ratio or ice water content (IWC). For that, a fast 3D fluid dynamical solver, based on semi-Lagrangian scheme (stable with large time step) was developed. Navier–Stokes equations are solved for an idealistic atmosphere (incompressible and inviscid) under the Boussinesq approximation and only evaporation and condensation are considered as adiabatic processes. Therefore, vapor mixing ratio, ice mixing ratio, potential temperature and the three components of wind are advected. Initial conditions are the vertical profile of pressure of ICAO (International Civil Aviation Organization) atmosphere, relative humidity (100% into cloud, 70% elsewhere), wind velocity and potential temperature whose vertical gradient sets the atmospheric layers stability. The initial perturbations of the 3D free divergence wind field are also fixed. They are non-random, as it is usually done, but are scale invariant with 1D spectral slope of $-\frac{5}{3}$, a fundamental property of free turbulence. This way of doing, speeds up the generation of cloud, as turbulence signature is injected directly from the departure of the simulation.
- The second step consists, firstly, in correcting the intensity of the 3D ice mixing ratio field in order to have a scale invariant field and, secondly, in mapping 3D ice mixing ratio or IWC fields into 3D optical depth field with the desired PDF and statistical properties. The control of the scale invariant property is done in Fourier space, by using the modulus of the energy and the phase; the control of the optical depth statistical

properties is done by a methodology close to the one proposed by [45]. Lot of cirrus characteristics can be found in the book “Cirrus” [46]. For the cirrus cloud studied in this paper, we chose a gamma distribution for the optical depth fields as in Smith and Del Genio [47] and as observed on in situ measurements. The optical thickness fields has a mean of 2, an inhomogeneous parameter ρ of 0.6 and a fractional cloud cover of 1. Note that the inhomogeneous parameter ρ is defined as the standard deviation of the 2D horizontal optical depth fields divided by its mean. In [47], it ranges from 0.4 to 1.5. A wind shear of $2\,\mathrm{m\,s^{-1}}$ is also added and as in Section 4, an IHM particles phase function is used for radiative transfer simulations.

The optical thickness of the cirrus cloud integrated along the z-axis is presented in Fig. 6a and the integration on the extinction coefficient along the Y-axis in Fig. 6b. Fig. 6c shows the power spectrum of the simulated fields that follows a power law with 1D spectral slopes close to $-\frac{5}{3}$ and Fig. 6d shows the gamma-like histogram of the 2D optical depth field integrated along z-axis.

5.2. Total and polarized reflectances for the 3D cirrus cloud

Radiative transfer calculations were done for a solar zenith angle of 60°. The medium is described by 128 × 128 × 44 pixels with a size of 78 m along the X- and Y-axis. Along the Z-axis, the pixel size is 78 m inside the cloud and 2 km outside the cloud to account for molecular scattering between 0 and 20 km. We assume a black underlying surface. The simulations were performed with 10^8 photons divided in 20 batches which allows

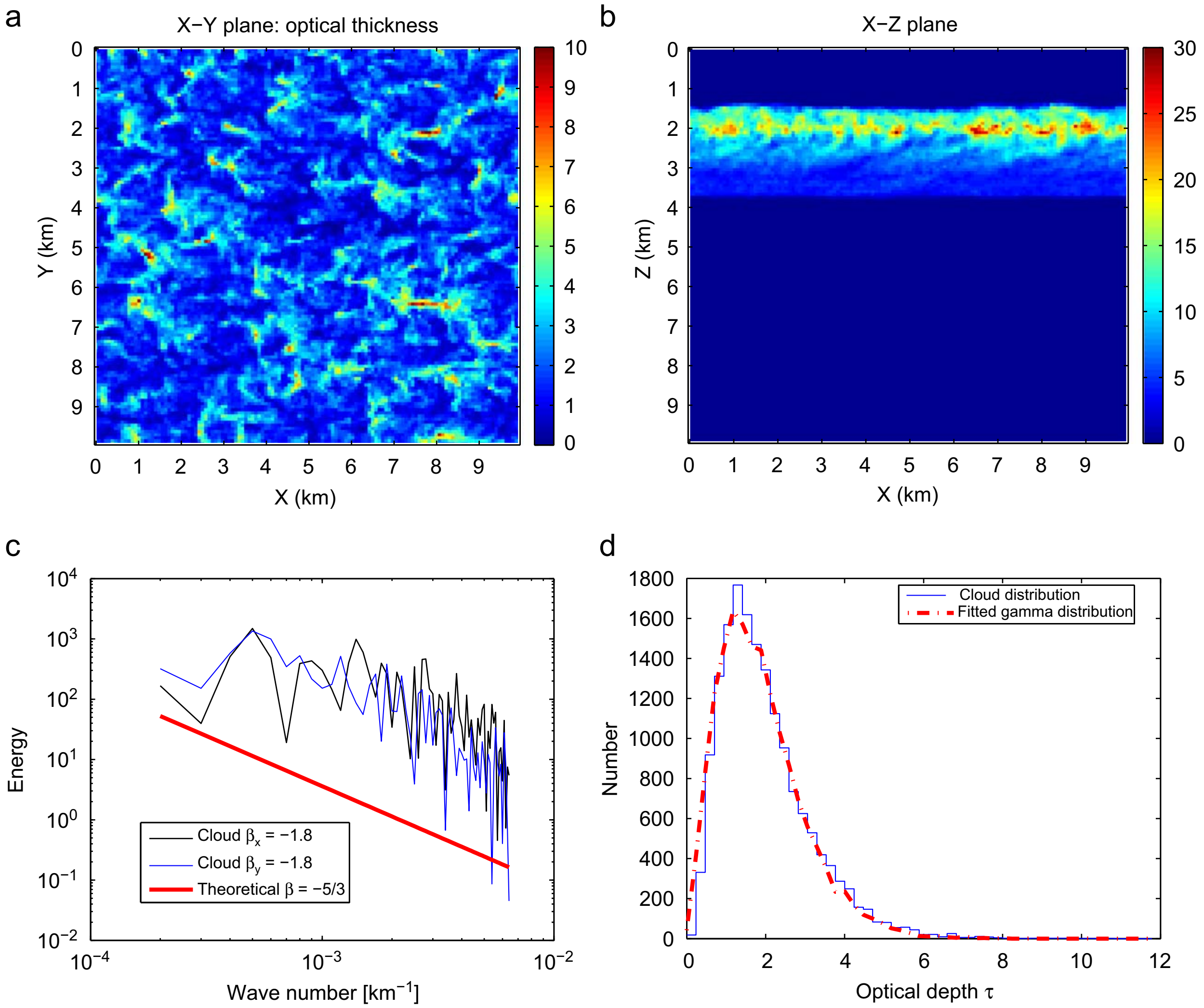

Fig. 6. Synthetic cirrus cloud used for the radiative transfer. The mean optical thickness is 2 and the cloud cover is 1. Optical thickness integrated along the z-axis (a), and along the Y-axis (b). (c) Energy power spectrum of the 2D vertically integrated optical depth as function of the wavenumber along the x-axis (black) and the y-axis (blue). In red is plotted the power spectrum of a theoretical signal with a spectral slope of $-\frac{5}{3}$ (isotropic turbulence). (d) Histogram of 2D cirrus optical depth field integrated along the z-axis. The fitted gamma distribution is also plotted. (For interpretation of the references to color in this figure legend, the reader is referred to the web version of this article.)

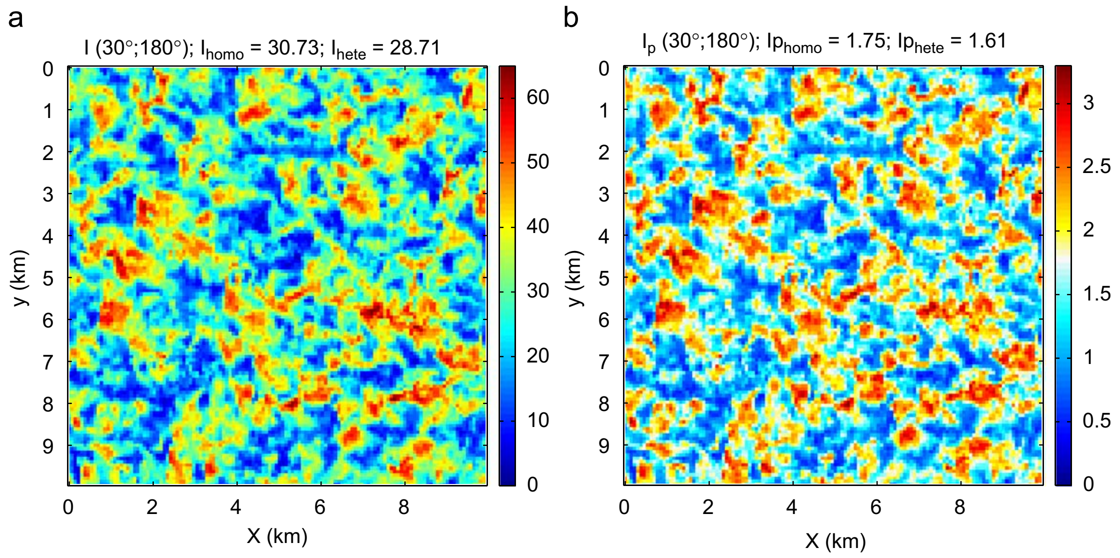

Fig. 7. Total (a) and polarized (b) reflectances in percent at 78 m resolution for $\theta_s = 60^\circ$; $\theta_v = 30$ and $\varphi_v = 180^\circ$ (forward scattering direction). The mean values are indicated above the figures for the 3D cirrus cloud (hete) and for the homogeneous cloud (homo).

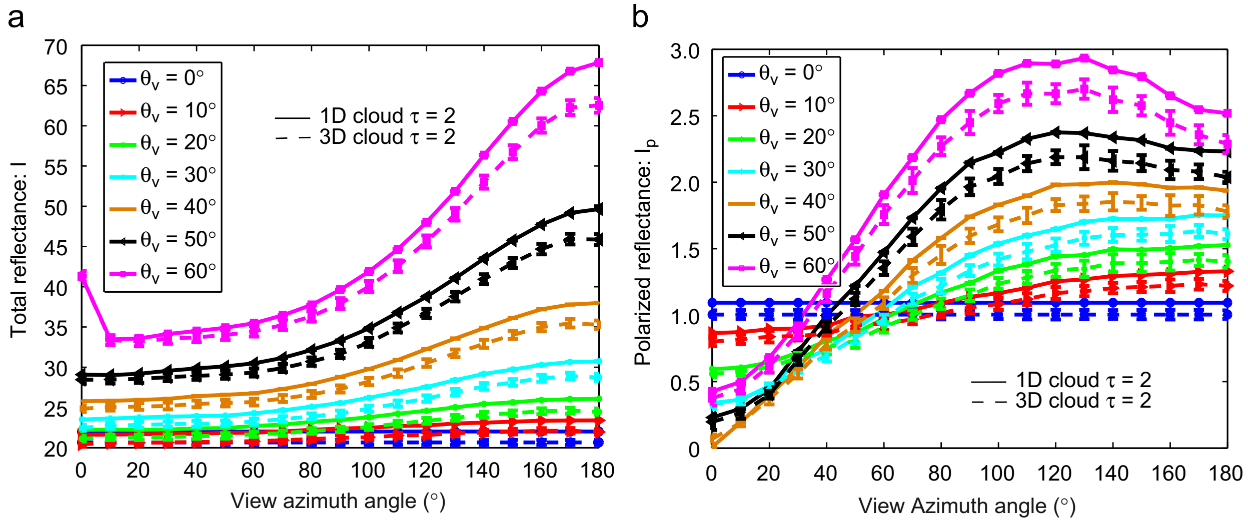

Fig. 8. Total (a) and polarized (b) mean reflectances in percent for $\theta_s = 60^\circ$ and for different zenith and azimuth angles. Solid lines are for a homogeneous cloud of optical thickness 2 and dashed lines for the cirrus cloud presented in Fig. 6. Error bars corresponds to the statistical error of Monte Carlo computations.

to compute the statistical error of the Monte Carlo calculations [7].

Results are presented in Figs. 7 and 8. Fig. 7 depicts total and polarized reflectances for a zenithal observation angle of 30° and a relative azimuth angle of 180° (forward scattering direction). Total reflectances point out the variability of the cloud field. In the same way, polarized reflectances presents lot of variability and very surprisingly, we notice that lots of pixels exhibit values of polarized reflectances much higher than the maximal value that can be reached with 1D computations. Due to saturation effects, this value is 1.90 (see Fig. 5). To emphasize this particularity, we reported in Fig. 5 the reflectances obtained for this 3D cloud in function of the optical thickness. Both total and polarized 3D reflectances are completely dispersed around the 1D relationship. This dispersion can be explained first because for oblique view, reflectances are the results of the energy coming along the slant path defined by the observation direction whereas the optical thickness is integrated along the vertical axis [48]. Another explanation can be that at high resolution the horizontal transport of the photons causes 3D effects called illumination and shadowing effects. They were already observed for total reflectances [48,49,23]. These effects, which enhance or reduce the reflectances, seems also affect the polarized reflectances and can thus lead to higher values that the one predicted by the 1D theory. Section 5.3 is dedicated to show how such high value of polarized reflectances can be reached and to check the hypothesis of illumination and shadowing effects.

A high spatial resolution of about 78 m corresponds to data such as airborne measurements. Measurements from space are at larger resolution in the order of the kilometer. To assess the sub-pixel heterogeneity effects, we average spatially the total and polarized reflectances fields to obtain values corresponding to 10×10 km pixel size, which is close to the POLDER pixel resolution. This spatial average of the total and polarized reflectances are presented for different zenithal observation angles as function of the relative azimuth angles, respectively, in Fig. 8a and b (dashed lines). In addition, as only 1-D codes are used to retrieve cloud properties from remote sensing data, we report also in Fig. 8a and b, the reflectance obtained from a 1-D model assuming the same microphysical model and an optical thickness of 2 (equal to the averaged optical thickness on the 3D domain). Error bars corresponding to the statistical errors of the Monte Carlo simulations are also plotted. In case of the polarized reflectances, we computed them from ΔQ and ΔU by

$$\Delta I_p = \frac{|Q\Delta Q| + |U\Delta U|}{I_p} \tag{25}$$

As expected due to the non-linearity of reflectances in function of the optical thickness and the so-called plane-parallel bias (Fig. 5, [39]), the 3D mean total reflectances are smaller than the corresponding 1D homogeneous reflectances for all the viewing angles. In Fig. 8b, we notice that this overestimation of reflectances under the 1D assumption exists also for the polarized reflectances. In this example, for total reflectances, the relative differences are between 0% and 8% and tend to increase with the azimuth angle. For polarized reflectances, the relative differences are about 7–8% for almost all the view directions. Note that error bars due to statistical error of the Monte Carlo computation allows to be sure of the significance of these differences as the error bars are smaller than the differences observed.

5.3. *Step cloud case: illumination and shadowing effects highlights*

To understand better illumination and shadowing effects on polarized reflectances, simulations were done for a simple cloud, a step cloud. The step cloud is here a flat cloud with two different optical thicknesses in one direction (X-direction) and infinite in the other direction (Y-direction). In our study, we choose an optical thickness of 0.5 for 128 continuous pixels of 78 m and 2 or 10 for the next 128 continuous pixels. Each continuous optical thickness domain has thus a length of about 10 km. Total and polarized reflectances obtained for a sun incidence of 60° and a zenithal observation angle of 30° in the forward direction ($\varphi = 180^\circ$) are presented, respectively, in Fig. 9a and b (sun illumination is coming from the left of the figure). Around 7 km where is the step in optical thickness, effect of illumination corresponding to an enhancement of the reflectances is clearly seen for total as well as for polarized reflectances. On contrary, near 17 km, we can see effect of shadowing which leads to a reduction of the reflectance values. Shadowing is often observed in everyday life so it is quite easy to understand. Note just that in case of clouds, it is not a complete cancelation of light but it corresponds just to its reduction due to the fact that light had passed through cloudy cells with non-negligible optical thickness. Illumination or brightness effect corresponds to the opposite effect: when an area of small optical thickness C_{τ_1} is adjacent to an area of larger optical thickness C_{τ_2}, photons pass over C_{τ_1} and increase the quantity of photons reaching C_{τ_2} comparing to an uniform cloud with only optical thickness τ_2. The number of photons reflected to the top by C_{τ_2} is thus more important. Outside these transition areas, the reflectance values corresponds to those of a homogeneous cloud and we notice again the saturation of the polarized reflectances with the same value for an optical thickness 2 or 10, which corresponds to the value given by the 1D model (1.90).

Concerning the brightness peak, one can notice that its shape is not the same for an optical thickness 2 or 10. It is quite logically higher for $\tau = 10$ than for $\tau = 2$ given the fact that more photons are stopped by areas of larger optical thickness. Moreover, we can notice that the peak is narrower for $\tau = 10$ in case of the polarized reflectances but also comparing to the brightness peak obtained for total reflectances. To explain this behavior, we show in Fig. 9c and d the successive contribution of the different orders of scattering for, respectively, total and polarized reflectances. For total reflectances, twenty orders of scattering are not sufficient to obtain the final reflectance values. On contrary, for polarized reflectances the values of the final reflectances is obtained after only four orders of scattering. This agrees with the fact that polarized signature is reached after few orders of scattering but also explains the change in the width of the peak. Indeed, as the number of scattering orders contributing to the final reflectances is limited in case of polarized reflectances, the difference in the geometrical photon free path in function of the optical thickness is more obvious, larger optical thicknesses leading to a larger number of photons reflected to the top along a shorter distance. Therefore, the peak for $\tau = 10$ is narrower and higher comparing to those for $\tau = 2$. In case of total reflectances, lot of orders of scattering contribute to the final response, which lead to broaden the brightness peaks.

To summarize, at high resolution, in the same way than total reflectances, polarized reflectances are very sensitive to 3D effects such as shadowing and illumination effects. Particularly, the latter effect can lead to value much higher than those predicted by the 1D theory. This can be very problematic for cloud properties retrieval, which assumes a 1D homogeneous cloud. Indeed, for total reflectances, illumination effects leads just, for example to an overestimation of the optical thickness but for polarized reflectances, one can meet situations with no solutions. However, as polarized reflectances depends of few orders of scattering, this enhancement or reduction of light is

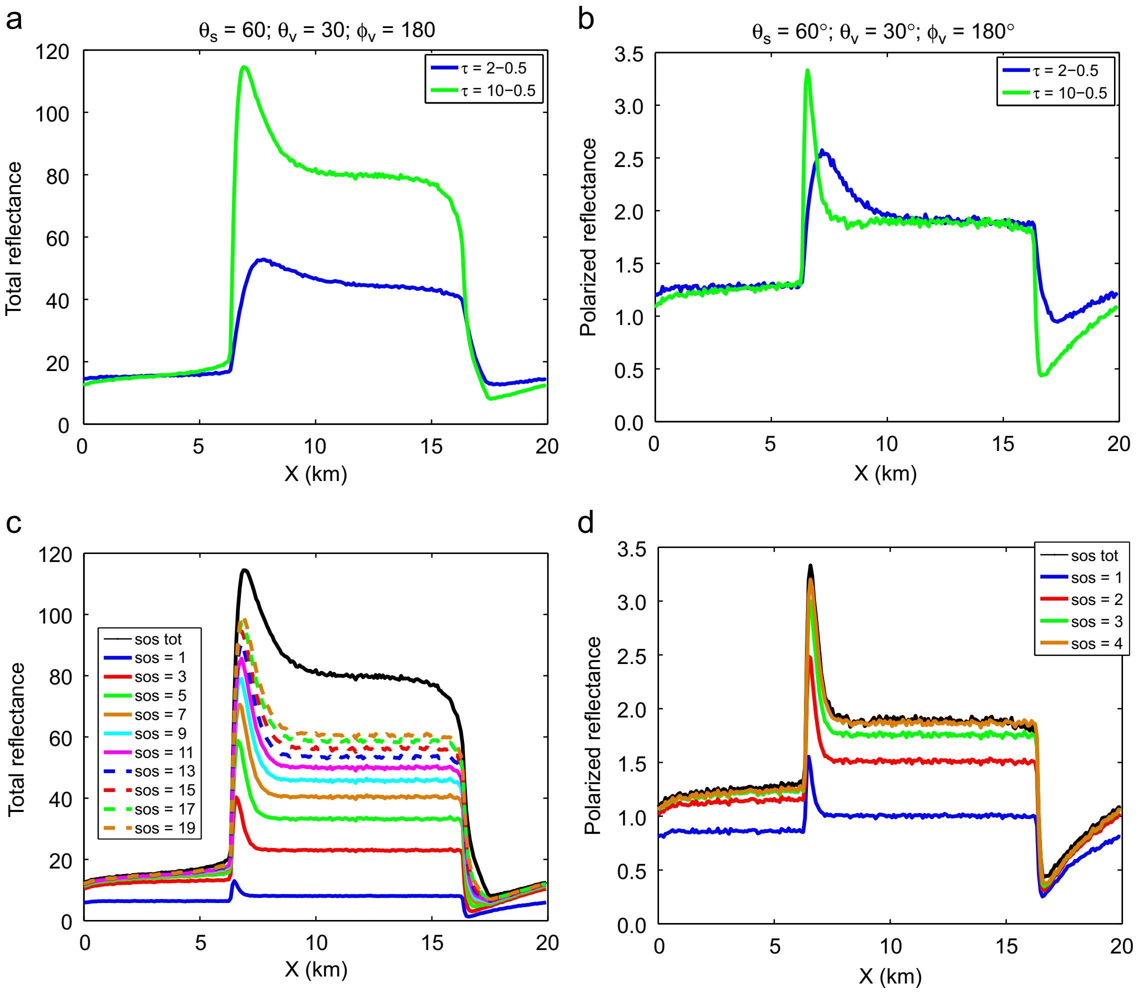

Fig. 9. Simulations done for step clouds with optical thickness 0.5 and 2 (blue line) or 0.5 and 10 (green line) for $\theta_s = 60^\circ$, $\theta_v = 30^\circ$ and $\varphi_v = 180^\circ$. (a) Total reflectances; (b) polarized reflectances; (c) successive contributions of the different orders of scattering for total reflectances for the case with optical thickness 0.5 and 10; and (d) same as (c) for polarized reflectances. In figures (c) and (d), the black lines represented the final reflectances corresponding to the results of the contribution of all the orders of scattering. (For interpretation of the references to color in this figure legend, the reader is referred to the web version of this article.)

spatially limited near cloud edges or exists principally when the optical thickness gradient is important.

6. Conclusions and perspectives

Modeling accurately radiative transfer inside the atmosphere is very important because remote sensing from space is increasingly used to obtain information on atmospheric components. In this work, we focus on one important property of atmosphere components that is the polarization of light. Polarized reflectances can be used to retrieve information on phase, size or shape of aerosol or cloud particles. Until now, operational algorithms used radiative transfer simulations based on the 1D homogeneous assumption to retrieve these atmospheric properties. In this work, we present a radiative transfer model based on Monte Carlo techniques which is able to model radiative transfer in a 3D medium accounting for the polarization state of light. The main difference between a polarized and non-polarized code concerns the computation of the Stokes parameters instead of only the total reflectance. In addition at each scattering event, the azimuth angle depends on the scattering zenith angle and on the state of polarization of the incident light and the rotation of the electric field need to be computed. This model has already been tested with no polarization in 3D cases and was validated, in this paper, with success for the polarization part on homogeneous cloud cases.

An example of 3D radiative transfer inside a cirrus cloud is presented. This cloud was created with a stochastic cloud model [43]. We analyzed the total and polarized reflectances and show that polarized reflectances are sensitive to 3D effects in a same way that total reflectances. At a medium resolution of 10 km, total as well as polarized reflectances are overestimated under the homogeneous assumption because of the so-called plane-parallel bias. At high resolution, with an oblique sun illumination, we observed 3D effects such as illumination and shadowing effects which, respectively, enhance or reduce the reflectances. Values higher than the ones predicted by the homogeneous assumption can thus be reached. These effects were highlight with the study of a step cloud and we noticed that the shape of the brightness peak depends on the horizontal optical thickness gradient.

In this paper, only one example was studied, works need to be pursued with other clouds including water clouds in order to determine the limitation of the 1D assumption in using multiangular polarized reflectances to detect the shape of ice particles or the size of liquid particles. For example, thanks to this new radiative transfer model, among other studies, it should be possible the study if macrophysical signature can be distinguished from microphysical ones. In the future, this model will also obviously be used in order to understand and to exploit better the polarized measurements that will be acquired by airbone or space sensors.

Acknowledgments

This research has been supported by the CNES, the CNRS, the University of Lille 1 and the French National Program of Teledetection Spatial (PNTS).

References

[1] Stamnes K, Tsay SC, Wiscombe WJ, Jayaweera K. Numerically stable algorithm for discrete-ordinate-method radiative transfer in multiple scattering and emitting media. Appl Opt 1988;27:2502–9.

[2] Rozanov W, Kokhanovsky AA. The solution of the vector radiative transfer equation using the discrete ordinates technique: selected applications. Atmos Res 2006;79:241–65.

[3] Hansen JE, Travis LD. Light scattering in planetary atmospheres. Space Sci Rev 1974;16:527–610.

[4] De Haan JF, Bosna PB, Hovenier JW. The adding method for multiple scattering calculations of polarized light. Astron Astrophys 1987; 183:371–91.

[5] Lenoble J, Herman M, Deuze JL, Lafrance B, Santer R, Tanre D. A successive order of scattering code for solving the vector equation of transfer in the earth's atmosphere with aerosols. J Quant Spectrosc Radiat Transfer 2007;107(3):479–507.

[6] Marchuk GI, Mikhailov GA, Nazaraliev MA, Darbinjan RA, Kargin BA, Elepov BS. The Monte Carlo method in atmospherics optics. New York: Springer; 1980.

[7] Evans KF, Marshak A. Numerical methods. In: Marshak A, Davis AB, editors. 3D radiative transfer in cloud atmospheres. Berlin: Springer; 2005 [chapter 4].

[8] Chandrasekar S. Radiative transfer. New York: Dover; 1960.

[9] Goloub P, Herman M, Chepfer H, Riedi J, Brogniez G, Couvert P, et al. Cloud thermodynamical phase classification from the POLDER spaceborne instrument. J Geophys Res 2000;105:14747–59.

[10] Riédi J, Goloub P, Marchand RT. Comparison of POLDER cloud phase retrievals to active remote sensors measurements at the ARM SGP site. Geophys Res Lett 2001;28:2185–8.

[11] Bréon F-M, Goloub P. Cloud droplet effective radius from spaceborne polarization measurements. Geophys Res Lett 1998;25: 1879–82.

[12] Bréon F-M, Doutriaux-Boucher M. A comparison of cloud droplet effective radii measured from space. IEEE Trans Geosci Remote Sens 2005;43:1796–805.

[13] Chepfer H, Goloub P, Riedi J, De Haan JF, Hovenier JW, Flamant PH. Ice crystal shapes in cirrus clouds derived from POLDER/ADEOS-1. J Geophys Res 2001;106:7955–66.

[14] Herman M, Deuze J-L, Marchant A, Roger B, Lallart P. Aerosol remote sensing from POLDER/ADEOS over the ocean: improved retrieval using a nonspherical particle model. J Geophys Res 2005;110: D10S02.

[15] Sun W, Loeb NG, Yang P. On the retrieval of ice cloud particle shapes from POLDER measurements. J Quant Spectrosc Radiat Transfer 2006;101:435–47.

[16] Deschamps P-Y, Breon F-M, Leroy M, Podaire A, Bricaud A, Buriez J-C, et al. The POLDER mission: instrument characteristics and scientific objectives. IEEE Trans Geosci Remote Sens 1994;32: 598–615.

[17] Auriol F, Léon J-F, Balois J-Y, Verwaerde C, François P, Riedi J, et al. Multidirectional visible and shortwave infrared polarimeter for atmospheric aerosol and cloud observation: OSIRIS (Observing System Including PolaRisation in the Solar Infrared Spectrum), vol. 7149, 2008.

[18] Mishchenko MI, Cairns B, Kopp G, Schueler CF, Fafaul BA, Hansen JE, et al. Accurate monitoring of terrestrial aerosols and total solar irradiance: introducing the glory mission. Bull Am Meteor Soc 2007;88:677–91.

[19] Loeb NG, Coakley JA. Inference of marine stratus cloud optical depths from satellite measurements: does 1D theory apply? J Clim 1998;11:215–33.

[20] Várnai T, Marshak A. Statistical analysis of the uncertainties in cloud optical depth retrievals caused by three-dimensional radiative effects. J Atmos Sci 2001;58:1540–8.

[21] Iwabuchi H, Hayasaka T. Effects of cloud horizontal inhomogeneity on the optical thickness retrieved from moderate-resolution satellite data. J Atmos Sci 2002;59:2227–42.

[22] Zinner T, Mayer B. Remote sensing of stratocumulus clouds: uncertainties and biases due to inhomogeneity. J Geophys Res 2006;111:D14209.

[23] Marshak A, Platnick S, Várnai T, Wen G, Cahalan RF. Impact of 3D radiative effects on satellite retrievals of cloud droplet sizes. J Geophys Res 2006;111:DO9207.

[24] Cornet C, Davies R. Use of MISR measurements to study the radiative transfer of an isolated convective cloud: implications for cloud optical thickness retrieval. J Geophys Res 2008;113:D04202.

[25] Marshak A, Davis AB. 3D radiative transfer in cloudy atmospheres. New York: Springer; 2005. p. 686.

[26] Buschmann N, McFarquhar GM, Heymsfield AJ. Effects of observed horizontal inhomogeneities within cirrus clouds on solar radiative transfer. J Geophys Res 2002;107:D4445.

[27] Carlin B, Fu Q, Lohmann U, Mace GG, Sassen K, Comstock JM. High-cloud horizontal inhomogeneity and solar albedo bias. J Clim 2002;15:2321–39.

[28] Schlimme I, Macke A, Reichardt J. The impact of ice crystal shapes, size distributions, and spatial structures of cirrus clouds on solar radiative fluxes. J Atmos Sci 2005;62:2274–83.

[29] Evans KF. The spherical harmonics discrete ordinate method for three-dimensional atmospheric radiative transfer. J Atmos Sci 1998;55:429–46.

[30] Ferlay N, Isaka H. Multiresolution analysis of radiative transfer through inhomogeneous media. Part I: theoretical development. J Atmos Sci 2006;63:1200–12.

[31] Mayer B. I3RC phase 1 results from the MYSTIC Monte Carlo model. Extended abstract for the I3RC (Intercomparison of 3D radiation codes) workshop, Tucson, Arizona, 1999.

[32] Iwabuchi H. Efficient Monte-Carlo methods for radiative transfer modeling. J Atmos Sci 2006;63:2324–39.

[33] Cahalan RF, Oreopoulos L, Marshak A, Evans KF, Davis AB, Pincus R, et al. The international intercomparison of 3D radiation codes (I3RC): bringing together the most advanced radiative transfer tools for cloudy atmospheres. Bull Am Meteor Soc 2005;86(9): 1275–93.

[34] Cashwell ED, Everett CJ. A practical manual on the Monte Carlo method for random walk problems. New York: Pergamon Press; 1959.

[35] House LL, Avery LW. The Monte Carlo technique applied to radiative transfer. J Quant Spectrosc Radiat Transfer 1969;9:1579–91.

[36] Ramella-Roman JC, Prahl SA, Jacques SL. Three Monte-Carlo programs of polarized light transport in scattering media: part I. Opt Express 2005;13:4420–38.

[37] Hovenier JW. Symmetry relationships for scattering of polarized light in a slab of randomly oriented particles. J Atmos Sci 1969;26:488–99.

[38] C-Labonnote L, Brogniez G, Buriez JC, Doutriaux-Boucher M, Gayet JF, Macke A. Polarized light scattering by inhomogeneous hexagonal monocrystals. Validation with ADEOS-POLDER measurements. J Geophys Res 2001;106:12139–53.

[39] Cahalan RF, Ridgway W, Wiscombe WJ, Bell TL, Snider JB. The albedo of fractal stratocumulus clouds. J Atmos Sci 1994;51: 2434–55.

[40] Evans KF, Wiscombe WJ. An algorithm for generating stochastic cloud fields from radar profile statistics. Atmos Res 2004;72: 263–89.

[41] Benassi A, Szczap F, Davis A, Masbou M, Cornet C, Bleuyard P. Thermal radiative fluxes through inhomogeneous cloud fields: a sensitivity study using a new stochastic cloud generator. Atmos Res 2004;72:291–315.

[42] Hogan RJ, Kew SF. A 3D stochastic cloud model for investigating the radiative properties of inhomogeneous cirrus clouds. Q J R Meteorol Soc 2005;131:2585–608.

[43] Szczap F. 3DCloud, a fast and flexible generator of optical properties of cirrus and stratocumulus/small cumulus based on simplified dynamical, thermodynamic and stochastic framework. ACPD, submitted for publication.

[44] Szczap F, Isaka H, Saute M, Guillemet B, Ioltukhovski A. Effective radiative properties of bounded cascade nonabsorbing clouds: definition of the equivalent homogeneous cloud approximation. J Geophys Res 2000;105(20):20617–34.

[45] Venema V, Meyer S, García SG, Kniffka A, Simmer C, Crewell S, et al. Surrogate cloud fields generated with the iterative amplitude adapted fourier transform algorithm. Tellus A 2006;58:104–20.

[46] Lynch DK, Sassen K, Starr D, Stephens G. Cirrus. Oxford: Oxford University Press; 2002. p. 504.

[47] Smith SA, Del Genio D. A simple conceptual model of cirrus horizontal inhomogeneity and cloud fraction. Q J R Meteorol Soc 2002;128:149–71.

[48] Várnai T, Davies R. Effects of cloud heterogeneities on shortwave radiation: comparison of cloud top variability and internal heterogeneity. J Atmos Sci 1999;56:4206–24.

[49] Várnai T, Marshak A. Observations of three-dimensional radiative effects that influence MODIS cloud optical thickness retrievals. J Atmos Sci 2002;59:1607–18.